This article has been accepted for publication in a future issue of this journal, but has not been fully edited. Content may change prior to final publication. Citation information: DOI 10.1109/JSTARS.2021.3085342, IEEE Journal of Selected Topics in Applied Earth Observations and Remote Sensing

Modeling daily temperatures via a phenology-based annual temperature cycle model

Haiping Xia[1], Yunhao Chen, Adu Gong, Kangning Li, Long Liang, Zhen Guo

***Abstract* — High-spatiotemporal-resolution land surface temperature (LST) plays an important role in various environment applications. However, the limitation of thermal infrared sensors and the effect of clouds and other atmospheric conditions result in discontinuous daily thermal observations of the Moderate Resolution Imaging Spectroradiometer (MODIS). Annual temperature cycle (ATC) models can help to supply daily continuous LSTs via limited observations, but these ATC models seldom consider the disturbance of weather conditions or the land cover change. On the other hand, spatial interpolation techniques also limit in implementation when available data in one day or several days are not able to obtain enough spatiotemporal information for LST reconstruction. The objective of this study is to propose a phenology-based ATC model (termed PATC), which takes the phenology change and local weather change into account, to reconstruct daily unscanned LSTs at an annual scale. Daily MODIS LSTs collected in 2015 were utilized to analyze the performance of PATC compared with other ATC models. Results show that PATC improved the accuracy by 1.6 K and 0.5 K compared to the classic ATC model in the daytime and nighttime, respectively. Compared to the enhanced ATC model (ATCE), PATC also shows better performance with higher accuracies, especially during the growing season of vegetation in the daytime. Future research may focus on an incorporation with Landsat observations and diurnal temperature cycle (DTC) models to implement LST reconstruction at a diurnal scale.**

***Index Terms*—Annual temperature cycle, phenology, LST reconstruction, MODIS.**

I. INTRODUCTION

Land surface temperature (LST), which estimated from satellite thermal infrared (TIR) sensors, is a key parameter in monitoring evapotranspiration [1], [2], modeling surface energy balance [3], analyzing urban heat island (UHI) effect [4], [5] and detecting thermal anomaly [6]. However, those TIR images are low tolerant to clouds which almost bring half missing data to the LST time series [7-10], accordingly affects the applications of LSTs on environmental analysis.

To fill out these spatiotemporal gaps, a number of spatial interpolation and temporal interpolation techniques were put forward. The spatial interpolation methods tend to be data-driven, and focus more on the spatial details on a specific date. According to the source of reference information, they can be generally grouped into two types: (1) spatial information based and (2) spatiotemporal information based. With the spatial information, the kriging geostatistical technique [11], inverse distance weighting (IDW) [12], and clustering inverse distance weighting (C-IDW) [13], could be applied for spatial interpolation. In addition, some auxiliary data such as NDVI and elevation were also utilized as predictors for regression to incorporate with the LST reconstruction process [14]. Fan *et al*. [15] even evaluated three regression tools and suggested that regression tree (RT) performed better than linear regression and artificial neural networks in flat and fragmented areas. However, spatial information from one day might not always be effective in some situations, hence, spatiotemporal information from adjacent dates was used to enable this interpolation. The spatiotemporal information based methods, such as the neighborhood similar pixel interpolator (NSPI) [16], geostatistical neighborhood similar pixel interpolator (GNSPI) [17], and weighted linear regression (WLR) algorithm [18] were proposed to make up for the insufficient of spatial information. These methods were not initially designed for LSTs so they seldom consider the characteristics of LSTs. Therefore, Shuai *et al*. [19] introduced the reflectance for similar pixels searching in the LST reconstruction process based on an assumption that the same land cover types have similar LST locally. Similarly, some spatiotemporal based interpolation methods aiming at LSTs were also implementing calculations via regression between multitemporal LSTs within similar pixels [20], [21].

Temporal interpolation methods are different from spatial interpolation methods in aims and principles, but they can be used for gap filling as well. Specifically, spatial interpolation methods designed for LSTs could utilize the spatiotemporal information from auxiliary data (e.g., multitemporal LSTs or NDVI), but they act less robustness when the gap is large [16], [22], [23]. On the contrary, temporal interpolation methods designed for LSTs (e.g., ATC models) can fully fill temporal gaps with several observations [23]. Some hybrid methods which combine temporal interpolation and spatial interpolation technique together, use temporal interpolation technique for gap filling instead, when missing data accounts for a large amount and the spatially interpolated result cannot meet with demand [24].

Temporal interpolation methods usually use sporadic observations to estimate consecutive data at different timescales [25]. Some of these temporal interpolation methods use singular spectrum analysis [26], temporal Fourier analysis [27], or a

[1] This work was supported by Beijing Natural Science Foundation (8192025), Projects of Beijing Advanced Innovation Center for Future Urban Design, Beijing University of Civil Engineering and Architecture (UDC2019031321) Beijing Laboratory of Water Resources Security, and by National Natural Science Foundation of China (41601468). (Corresponding author: Yunhao Chen and Adu Gong.)
H. Xia, Y. Chen, K. Li, and L. Liang are affiliated with the State Key Laboratory of Remote Sensing Science, Faculty of Geographical Science, Faculty of Geographical Science, Beijing Normal University, Beijing 100875, China (e-mail: xiahp93@mail.bnu.edu.cn; cyh@bnu.edu.cn; gad@bnu.edu.cn; lknkiki@mail.bnu.edu.cn; lianglong@mail.bnu.edu.cn).
Z. Guo is with the National Satellite Meteorological Center, Beijing 100081, China (e-mail: guozheng@cma.gov.cn).

This article has been accepted for publication in a future issue of this journal, but has not been fully edited. Content may change prior to final publication. Citation information: DOI 10.1109/JSTARS.2021.3085342, IEEE Journal of Selected Topics in Applied Earth Observations and Remote Sensing

principal component analysis (PCA) [28] for data reconstruction, of which many of them were not initially designed for LSTs. In addition, most of these temporal interpolation methods rely on the physical or statistical models to describe the temporal variations of temperatures [28-31]. Specifically, at a diurnal timescale, various diurnal temperature cycle (DTC) models which consist of several parameters are used for temperature modeling [32-38]. While at an annual timescale, annual temperature cycle (ATC) models [29], [31] play an important role in the temporal interpolation processes instead. Moreover, the annual predictions can also serve for diurnal temporal interpolations [35], thermal sharpening [39], [40] and analyzing of UHIs [4], [41] and public health [42].

The ATC models used to predict daily LSTs can be generally divided into two groups. The first group requires only the multitemporal temperature observations, which consists of one or two sine functions [43], [44], or even a series of harmonic functions [30]. There are some methods incorporating an ATC model with a linear trend for multi-year LST modeling can also be classified into this group [43], [45]. These algorithms are designed based on the LST without any other auxiliary data, and they have common in the assumption that the temporal variation of LSTs is primarily driven by the solar radiation [29], [30], [44]. The second group uses not only multitemporal LSTs, but also a series of auxiliary data such as the in-situ surface air temperature (SAT), normalized difference vegetation index (NDVI) and albedo [23], [46] to take the local synoptic conditions and land cover change into account. This kind of methods are combinations of multiple harmonics and a linear function of LST-related factors, which can help the model adapt to different scenarios [23]. However, existing ATC models seldom consider the response of vegetation to phenology in mixed pixels, when the observed object consists of vegetation which has significant phenological changes in a year (e.g., turning green or turning brown), single or multiple harmonics, even those linear regression model may not be able to simulate the daily temperature variation well.

Therefore, the objective of this study is to propose a phenology-based ATC model (termed PATC) for time series LST reconstruction, which takes the response of vegetation to phenology into account. Here, we used daily day/night LSTs of the Moderate Resolution Imaging Spectroradiometer (MODIS) to implement this method. Study area and data are provided in Section II. The details of the method and implementation process are provided in Section III. Results and discussions are presented in Section IV and V, while conclusion in Section VI.

II. STUDY AREA AND DATA

A. Study area

Beijing, Tianjin and Hebei province, located in the North China Plain with a semi-humid continental monsoon climate are selected as the study area. Specifically, this study area has a rainy and hot summer and a dry and cold winter, whose spring and autumn are extremely short. The study area (see in Fig. 1(b)) is mainly covered by cropland and grassland, and the elevation ranges from -6 m to 2764 m with a mean elevation of 506 m. Since the land cover consists of large amount of vegetation and the four seasons are distinct in this study area, the phenology changes significantly. These characteristics make this study area an ideal place to test the model performance at a regional scale.

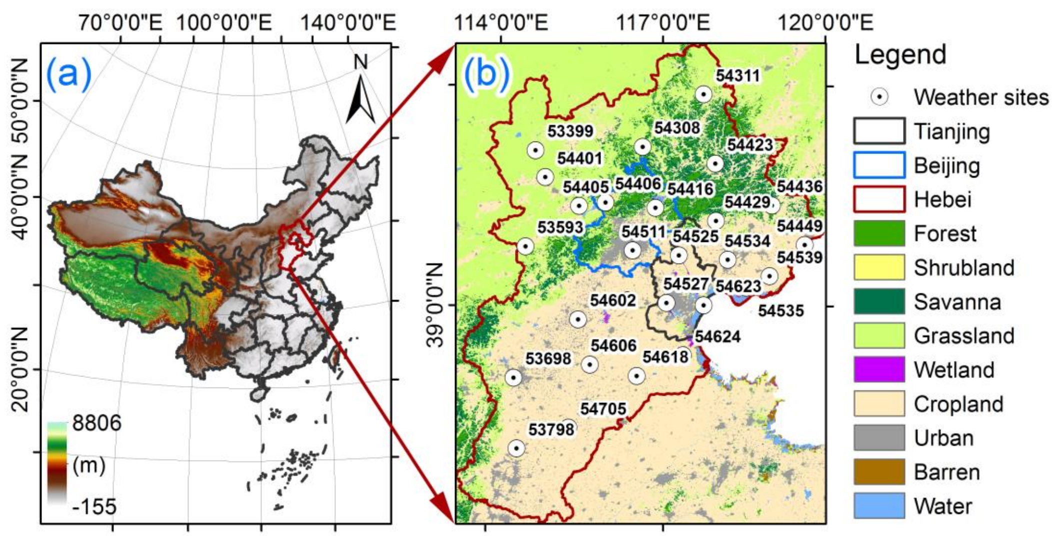

Fig. 1. Study area. (a) DEM of China; (b) Land cover map of Beijing, Tianjin and Hebei Province (obtained from MODIS yearly land cover product in 2015).

B. Data

The satellite data used in this study include the MODIS daily LST product MOD11A1, 16-day NDVI product MOD13A2, and the MODIS yearly land cover product MCD12Q1 in 2015 (download from https://ladsweb.modaps.eosdis.nasa.gov/). Specifically, the MODIS LSTs in collection 6 were retrieved via the generalized split-window algorithm with a mean error within 1.0 K which were proved to be better than the previous C4.1 and C5 products [47-49]. The daytime and nighttime LSTs of the MOD11A1 were acquired at around 10:30 am and 10:30 pm, respectively. In addition, the Shuttle Radar Topography Mission (STRM) digital elevation model (DEM) image with a resolution of 90 m was download from http://www.gscloud.cn/. The resolutions of the MOD13A2, DEM and MCD12Q1 were resampled to 1 km to match that of the LST product. Moreover, the NDVI product derived from the MOD13A2 is a 16-day

This article has been accepted for publication in a future issue of this journal, but has not been fully edited. Content may change prior to final publication. Citation information: DOI 10.1109/JSTARS.2021.3085342, IEEE Journal of Selected Topics in Applied Earth Observations and Remote Sensing

composite, hence, we applied a thin plate spline (TPS) interpolation to make it daily available.

Apart from those satellite data, daily maximum and minimum SATs from 27 meteorological stations (see Fig. 1(b)) download from http://data.cma.cn/site/ were also used here. These SATs were resampled into 1 km-resolution raster images via IDW method to match the LST products [46].

III. METHOD

In this section, we first introduce the classic ATC model and the enhanced ATC model (ATCE), then we provide a detailed description of PATC. The model diagram and flowchart of PATC is provided in Fig. 2.

A. The classic ATC model

The temporal interpolation of PATC is composed of various ATC models. Here, we utilize the classic ATC model which is consist of three parameters [29] and we term it ATC in this study. The equation of ATC is as follow:

$$\varphi_{ATC}(T_0, A, \theta, d) = T_0 + A \cdot sin(2\pi d/365 + \theta) \tag{1}$$

where φ_{ATC} is the predicted LST via the ATC model, d represents the day of the year (DOY), T_0, A and θ are the mean LST, amplitude and phase shift of the annual LST cycle, respectively. These parameters are obtained via a Levenberg-Marquardt scheme [50] in the IDL platform.

Since the ATC model tends to smooth LSTs temporally [23], there are always residuals remained between the observations and predictions. Hence, the observed LSTs can be expressed as,

$$T(d) = \varphi_{ATC}(T_0, A, \theta, d) + \Delta T(d) \tag{2}$$

where $T(d)$ is the observed LST on the *d*th day, and $\Delta T(d)$ is the residual between the observation and the prediction on the *d*th day.

B. The enhanced ATC model (ATCE)

The enhanced ATC model assumes that the annual surface temperature dynamics are mainly controlled by the solar radiation flux at the top of the atmosphere. In addition to solar radiation, the surface temperature is also controlled by the climatic background and local weather conditions, leading to short-term fluctuations of the surface temperature [46]. Therefore, the model can be expressed as follows:

$$T_{ATCE}(d) = T_0 + A \cdot sin\left(\frac{2\pi d}{365} + \theta\right) + \Delta T_{air}(d) \cdot \gamma(d) \tag{3}$$

where $T_{ATCE}(d)$ is predicted LST on the *d*th day, ΔT_{air} is the temperature fluctuations caused by weather conditions, $\gamma(d)$ is the phenological factor, and can be expressed by following equation:

$$\gamma(d) = \lambda \cdot (NDVI_{max} - NDVI_{min})/[NDVI(d) - NDVI_{min} + 1] \tag{4}$$

where λ is the multiplier factor, $NDVI_{min}$ and $NDVI_{max}$ are the minimum and maximum NDVI values in a year, respectively; $NDVI(d)$ is the NDVI value on the *d*th day. In addition, the air temperature fluctuations can be calculated by following equation:

$$\Delta T_{air}(d) = T_{air}(d) - T_{ATC,air}(d) \tag{5}$$

where $T_{air}(d)$ is the maximum/minimum air temperature on the *d*th day, $T_{ATC,air}(d)$ is the maximum/minimum air temperature simulated by ATC model, which can be calculated by Equation (1). Specifically, the maximum air temperature is used for calculation in the daytime while the minimum air temperature in the nighttime.

C. The phenology-based ATC model (PATC)

Due to the heterogeneity of the land surface, when the thermal signal in an endmember is smaller than the pixel size, the pixel will respond to the thermal signal of multiple endmembers [35], and the mixing effect of the pixel will be enhanced with the reduction of resolution. The linear temperature mixing model (LTMM) assumes that the temperature of the mixed pixel is a weighted linear combination of different endmember components [51]. Therefore, considering the mixing effect of pixels, the PATC assumes that the surface temperature of a pixel is a linearly weighted combination of vegetated and non-vegetated fractions. In addition, considering the influence of local weather, the PATC also regresses surface temperature fluctuations caused by weather conditions and air temperature fluctuations for temperature reconstruction (see in Fig. 2). Therefore, the formula of PATC, which takes both phenological changes and local weather effects into account, is as follows:

$$T_{PATC}(d) = f_v(d) \cdot \left[T_{v,0} + A_v \cdot sin\left(\frac{2\pi d}{365} + \theta_v\right)\right] + f_{nov}(d) \cdot \left[T_{nov,0} + A_{nov} \cdot sin\left(\frac{2\pi d}{365} + \theta_{nov}\right)\right] + \Delta T(d) \tag{6}$$

where $T_{PATC}(d)$ is the predicted LST via PATC on the *d*th day, f_v is the fraction of vegetation in a mixed pixel, f_{nov} is fraction of non-vegetation in a mixed pixel, and it can be calculated by $f_{nov} = 1 - f_v$; $T_{v,0}$, A_v and θ_v are the annual mean temperature, amplitude and phase of the vegetation fraction, respectively, $T_{nov,0}$, A_{nov} and θ_{nov} are the annual mean temperature, amplitude and phase of the non-vegetation fraction, respectively; ΔT is the fluctuations of LST, and it can be obtained through the statistical regression with temperature fluctuations, the equation is as follow:

$$\Delta T(d) = k \cdot \Delta T_{air}(d) + b \tag{7}$$

where k and b are the slope and the intercept, ΔT_{air} is the fluctuation of air temperature, and can be calculated by Equation (5).

Meanwhile, the vegetation fraction can be calculated by Equation (8):

$$f_v = \left(\frac{NDVI - NDVI_{min}}{NDVI_{max} - NDVI_{min}}\right) \tag{8}$$

where $NDVI_{min}$ and $NDVI_{max}$ are the minimum and maximum NDVI value, respectively.

Since MODIS products only provide 16-day synthetic NDVI and are subject to weather conditions (such as cloud and atmospheric disturbances), NDVI products for different dates have different noise levels. Therefore, the changing-weight filter method (CWF) [52] is adopted in this study to remove noise of the NDVI products. After removing noise, spline interpolation was used to obtain daily NDVI data. The flowchart can be seen in Fig. 2.

This article has been accepted for publication in a future issue of this journal, but has not been fully edited. Content may change prior to final publication. Citation information: DOI 10.1109/JSTARS.2021.3085342, IEEE Journal of Selected Topics in Applied Earth Observations and Remote Sensing

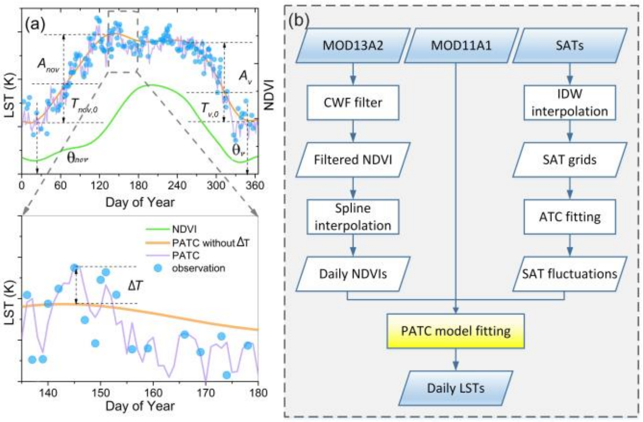

Fig. 2. Model diagram and flowchart of PATC. (a): model diagram of PATC; (b) flowchart of PATC.

IV. RESULT

A. Spatial and temporal patterns of PATC

In this section, we present the spatial and temporal patterns of PATC and compare them with the classic ATC model. The evaluation indicators used in this study include root mean square error (RMSE) and difference of RMSE (Drmse). Compared with classic ATC, PATC performs better in both daytime and nighttime with a lower RMSE of 3.1 K for the daytime and 2.5 K for the nighttime, while those of classic ATC are 4.7 K for the daytime and 3.0 K for the nighttime. The higher RMSEs of both PATC and ATC in the daytime compared to those in nighttime might due to the higher LST variations during daytime [46]. As shown in Fig. 3, the RMSEs of classic ATC are higher in the northern area of which the land cover type is mainly grassland and terrain is complex, and lower in the southern area of which the land cover type is mainly cropland and the terrain is flat. The spatial pattern of PATC's RMSEs is similar to that of classic ATC, of which the RMSEs are slightly lower in the southeast of the study area and higher in the northwest. However, the Drmse (referenced to classic ATC) of PATC is higher in the northern area, which indicates a higher improvement in areas covered by grassland and wherein the terrain is complex (see in Fig. 3(c)&(f)). In addition, the temperature difference of vegetation and bare soil components in mixed pixels is larger in the daytime than that in the nighttime, which decreases the accuracy of the temperature cycle model in the daytime. The Drmse in the nighttime is also lower than that in the daytime with a mean value of 0.5 K, which is due to the more homogeneous land surface temperature in the nighttime (see in Fig. 3(c)&(f)).

To evaluate the improved accuracy of PATC evaluated via Drmse (referenced to classic ATC) response to land cover types, the classified Drmses are provided in Fig. 4. Results show the improvements over grassland are higher than over other land covers in both daytime and nighttime. In the daytime, the grassland presents the largest mean Drmse of 2.0 K, while the urban area presents the lowest with 1.2 K, and the mean Drmses of cropland, forest and savanna are 1.4 K, 1.8 K and 1.7 K, respectively. In the nighttime, the difference of Drmses of various land cover types is smaller, that almost of them are at around 0.5 K, wherein the Drmses of grassland is slightly higher. The lower Drmses in the nighttime is because the temperature difference between vegetation and non-vegetation fractions is larger in the daytime than that in the nighttime, accordingly, the superiority of the application of LTMM in the nighttime is not as obvious as that in the daytime.

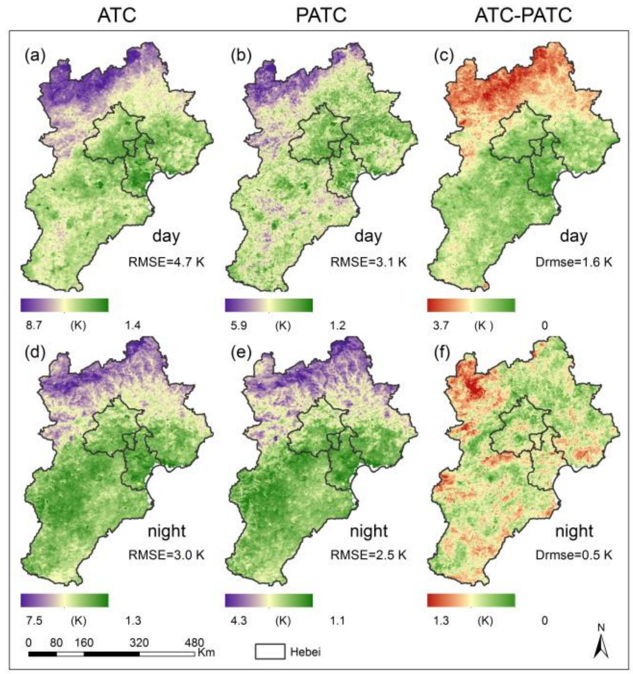

Fig. 3. RMSEs of classic ATC and PATC, and Drmse of PATC (referenced to classic ATC) in daytime and nighttime, respectively.

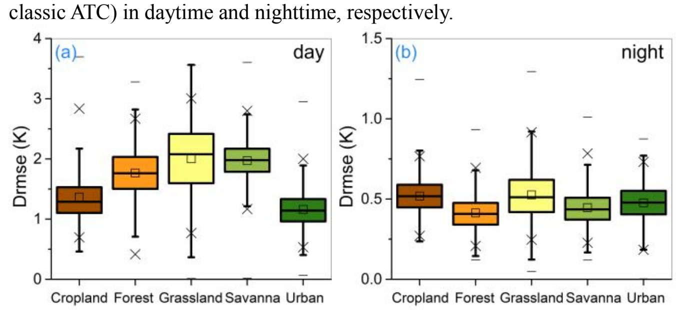

Fig. 4. Drmse of PATC (referenced to classic ATC) over different land cover types in daytime and nighttime, respectively.

Above results show the spatial pattern of the performance of PATC. To evaluate the performance of PATC temporally, three pixels located in three different land cover types are selected to show the results of PATC, the land covers of which are grassland, cropland and forest, respectively. Here, we also supply NDVI variation corresponding to the LSTs to explain the fluctuation of LST observations. As show in Fig. 5, the predicted LST via PATC can reliably catch the short-term variations of LSTs caused by the weather change and phenology change, while that via classic ATC tends to smooth these fluctuations. For example, as shown in Fig. 5(a2), the vegetation fraction in the mixed pixel increases when the grassland starts growing, hence, the temperature of the mixed pixel decreases by the transpiration of vegetation in the daytime [53]. Meanwhile, the ATC curve cannot totally catch the variations of observations and the RMSE of which is 6.3 K, while PATC curve fits these observations quite well and the RMSE of which is 3.2 K (Fig. (5a)). As shown in Fig. 5(c), in

This article has been accepted for publication in a future issue of this journal, but has not been fully edited. Content may change prior to final publication. Citation information: DOI 10.1109/JSTARS.2021.3085342, IEEE Journal of Selected Topics in Applied Earth Observations and Remote Sensing

the cropland, the vegetation fraction starts to decrease when the vegetation enters its first end of season (EOS), hence, the LST of the mixed pixel is improved due to the highly reflected sunlight in the daytime. Meanwhile, the temperature fluctuations are well simulated by PATC of which the RMSE is improved by 1.3 K compared with the classic ATC model. On the contrary, the vegetation fraction will not cool the surface [54], but increases the LST [55] in the nighttime. Specifically, the decreased vegetation fraction of the cropland decreases the LST in the nighttime during its first EOS. The temperature fluctuation is not as evident as that in the daytime, but it still can be caught by PATC (see in Fig. 5(d1)). As shown in Fig. 5(e), in the forest, the LST decreases due to the cooling effect of vegetation when the vegetation fraction reaches to 1, the temperature fluctuation of which is well predicted by PATC model, while is overestimated by the classic ATC model. The effect of phenology changes on LST is smaller in the nighttime than in the daytime, therefore, the PATC model improves less RMSE compared with classic ATC at night, the improved RMSEs of grassland, cropland and forest are 0.7 K, 0.6 K and 0.3 K, respectively (see in Fig. 5). In addition to the LST variations caused by the phenology change, PATC can also catch the short-term LSTs fluctuation caused by local weather change. As shown in Fig. 5(a1), PATC model better simulates the temperature fluctuations caused by local weather changes, the temperature fluctuations at night are smaller but can also be captured by PATC (see in Fig. 5(b)).

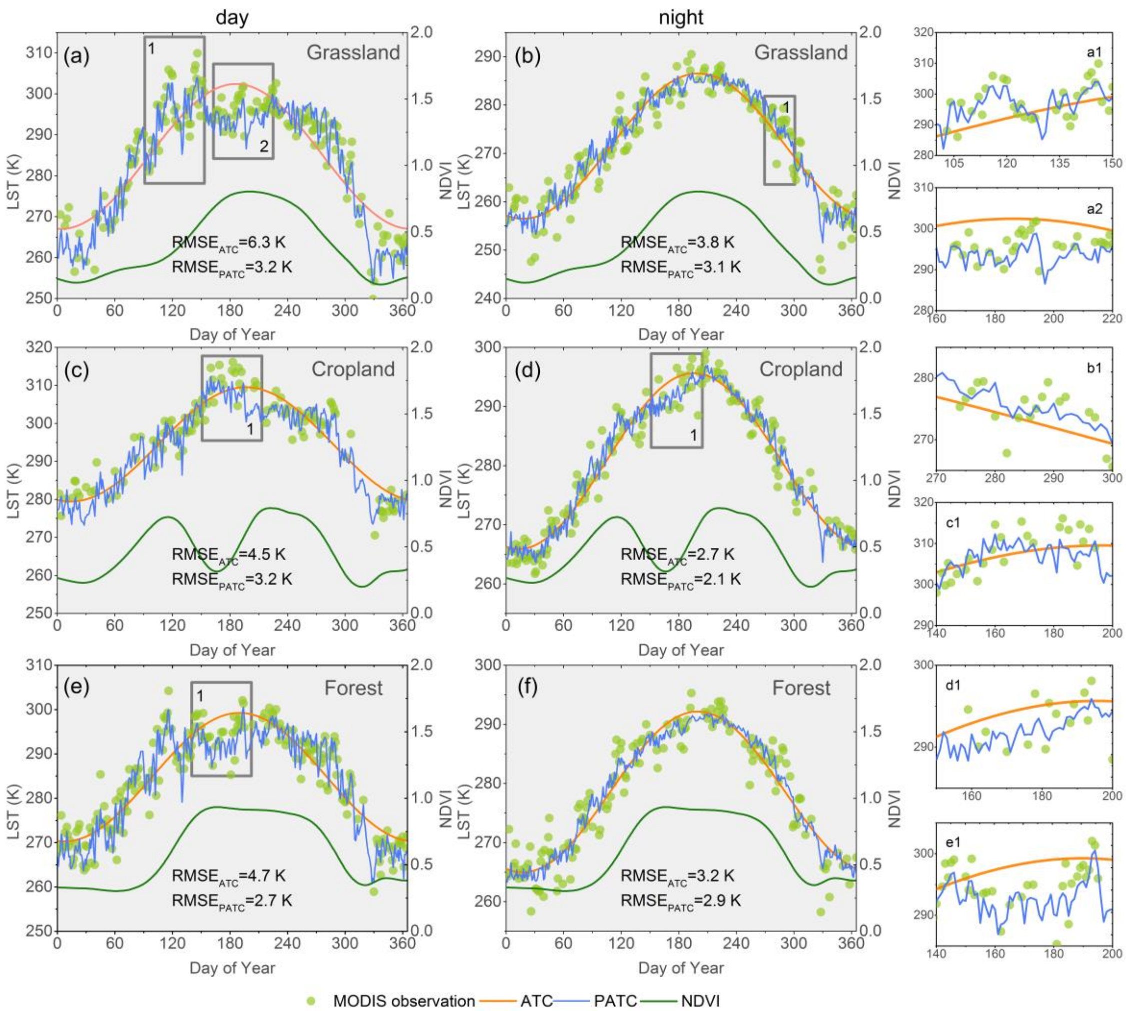

Fig. 5. Comparisons of model performances of PATC and classic ATC at daily scale in daytime and nighttime. (a1), (a2), (b1), (c1), (d1) and (e1) are the subfigures from the first and second columns. The $RMSE_{ATC}$ and $RMSE_{PATC}$ represent the RMSEs of classic ATC and PATC, respectively.

B. Accuracy improvement compared with ATCE

PATC and ATCE model take the same data as input, and both take the effects of phenology change and weather condition on LSTs into account. The main difference between two models is that PATC is based on a LTMM [35], [51], which separates the effects of phenology change and weather conditions, while ATCE combines the effects of phenology change and weather conditions together [46]. Here, we compare PATC with ATCE via the evaluation indicator of Drmse (referenced to ATCE) to explore whether the LTMM-based PATC model is superior to ATCE, wherein a higher Drmse value indicates better performance of PATC compared with ATCE. In this section, we calculate different Drmses among different NDVI ranges. Specifically, time series observations are classified by different NDVI ranges to calculate Drmses.

Different Drmses corresponding to different NDVI ranges indicate that PATC performs better than ATCE, with a mean Drmse value of 0.3 K and 0.1 K in the daytime and nighttime, respectively. As shown in Fig. 6(a), in all land covers types, the predicted LSTs of which the corresponding NDVI values ranging from 0.8 to 1.0 have higher Drmses than other predictions in the daytime, the mean Drmses of urban, cropland, grassland, forest and savanna are 2.4 K, 2.2 K, 1.3 K, 0.7 K and 0.8 K, respectively. When the NDVI values range from 0.6 to 0.8, the Drmses of urban, cropland and grassland are still higher than predictions of which the corresponding NDVI values are less than 0.6. When the NDVI value ranges from 0 to 0.2, the Drmses of cropland and grassland are lower than those of which the NDVI is larger than 0.6 but are still slightly higher than those of which the NDVI value is ranging from 0.2 to 0.6. Therefore, we can summarize that a higher NDVI value indicates a higher improvement of PATC compared with ATCE in the daytime, however, when the NDVI value is less than 0.2, PATC still performs better than ATCE with a mean Drmse of 0.5 K.

The superiority of PATC compared with ATCE in the nighttime is not as obvious as that in the daytime. As shown in Fig. 6(b), the mean Drmse of all land cover types is only 0.1 K, and the Drmses of all land cover almost keep the same in different NDVI ranges. However, when the NDVI values are less than 0.2, forest and savanna have a higher Drmse than other land cover types, which might due to the proportions of these two types are quite low. Moreover, the lower improvement of PATC compared with ATCE in the nighttime is because both PATC and ATCE consider the effect of local weather, so they can simulate the local fluctuations caused by weather conditions in nighttime. However, the difference of LST between nocturnal vegetation and bare soil is small, so the mixed pixel LST is less affected by vegetation phenology changes.

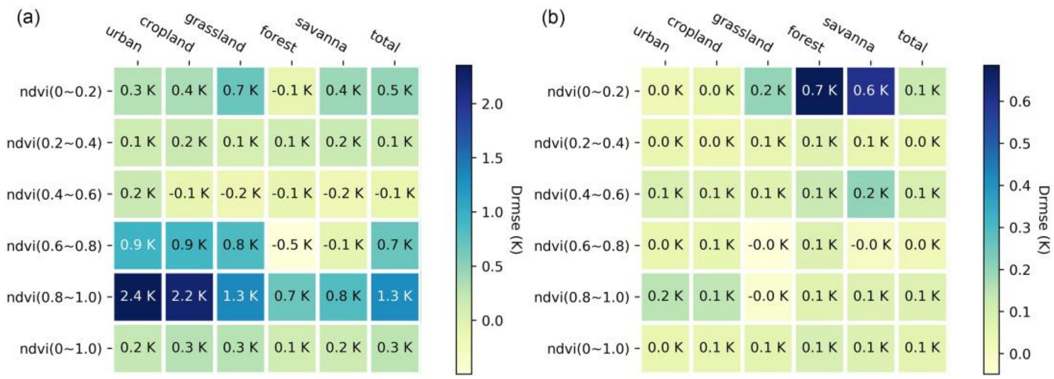

Fig. 6. Drmse (referenced to ATCE) of PATC over different land cover types in daytime and nighttime, respectively. (a): Drmse in daytime; (b) Drmse in nighttime.

To explore the spatial distribution of Drmses in different NDVI ranges in the daytime, we also supply the spatial patterns of Drmse. As shown in Fig. 7(f), the mean Drmse of all predictions is 0.3 K, and the higher Drmse occurs in the northwest and southwest of the study area of which the land cover types are mainly grassland and cropland. As shown in Fig. 7(a), when the NDVI value is less than 0.2, there are some pixels that lack of observations and these pixels are mainly cropland and forest. The mean Drmse is 0.5 K which indicates a satisfying improvement of PATC compared with ATCE, moreover, the higher Drmses locate in the northwest of this study area are mainly grassland, the maximum even reaches to 6.1 K (see in Fig. 7(a)). When the NDVI values range from 0.2 to 0.4, the improvement of PATC is unobvious, the mean Drmse is only 0.1 K, and higher Drmses mainly occur in cropland, the maximum Drmse is only 2.1 K (see in Fig. 7(b)). When the NDVI values range from 0.4 to 0.6, PATC even performs poorer than ATCE, the mean Drmse is -0.1 K (see in Fig. 7(c)). However, when the NDVI value is larger than 0.6, the superiority of PATC compared with ATCE is obvious. As shown in Fig. 7(d)-(e), when the NDVI values range from 0.6 to 0.8, the mean Drmse is 0.7 K, and the maximum Drmse reaches to 7.1 K; when the NDVI values range from 0.8 to 1.0, the mean Drmse is 1.3 K, and the higher Drmses mainly occur in cropland and grassland. In summary, PATC performs better than ATCE in most situations, especially when the NDVI is larger than 0.6, but slightly poorer when the NDVI value ranges from 0.4 to 0.8.

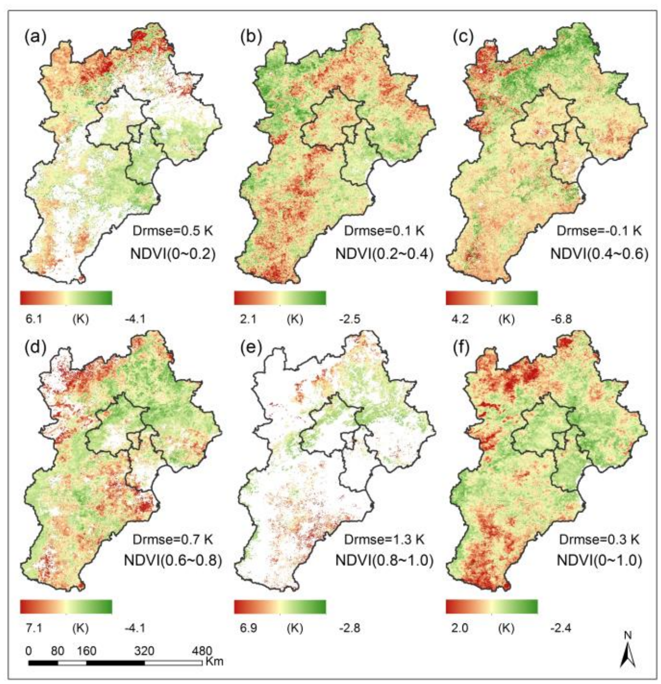

Fig. 7. Drmse (referenced to ATCE) of PATC in the daytime. (a)-(e) are the Drmses corresponding to different NDVI ranges.

In addition to comparing Drmses among different NDVI ranges, we also want to explore the relationship between Drmse and annual change rate of NDVI. Here, we use the annual mean derivate of NDVI (NDVI') to represent the annual change rate of NDVI, of which a larger value indicates a more complex

This article has been accepted for publication in a future issue of this journal, but has not been fully edited. Content may change prior to final publication. Citation information: DOI 10.1109/JSTARS.2021.3085342, IEEE Journal of Selected Topics in Applied Earth Observations and Remote Sensing

annual change of NDVI. As shown in Fig. 8, Drmse is positively correlated with the annual mean derivate of NDVI in both daytime and nighttime. However, the slope of their relationship is larger in the daytime and smaller in the nighttime, with value of 0.99 for the daytime and 0.03 for the nighttime. The results indicate that the phenology change has a larger influence on PATC in the daytime than in nighttime. Moreover, the more complex the phenology change, the superior the performance of PATC compared with that of ATCE.

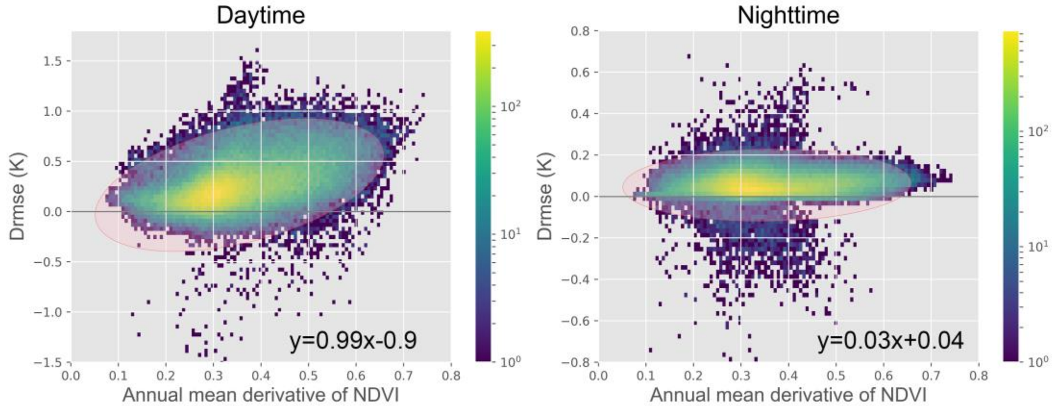

Fig. 8. Scatter plot between Drmse (referenced to ATCE) and the annual mean derivative of NDVI in the daytime and nighttime, respectively.

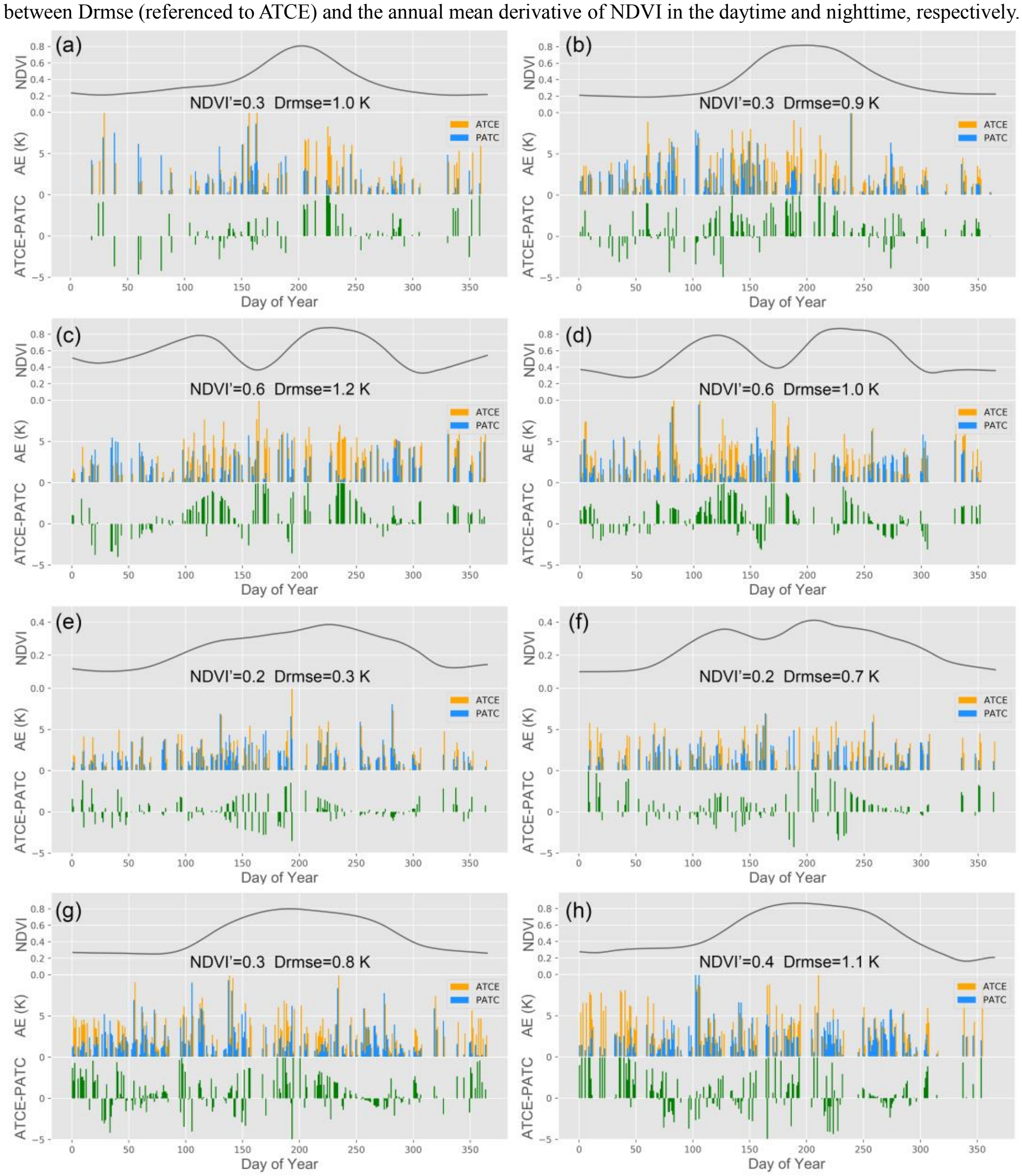

Fig. 9. Comparisons of model performances of PATC and ATCE in daytime. (a)-(d): cropland; (e)-(f): urban; (g)-(h): grassland.

To compare PATC and ATCE temporally, we selected eight pixels with different phenology changes to show their daily absolute error (AE). As shown in Fig. 9(a), when the cropland enters its start of season (SOS) in the early summer, the difference between the AEs of ATCE and PATC begins to increase; and when the cropland enters its EOS in autumn, the difference between the AEs of ATCE and PATC begins to decrease, which indicates a better performance of PATC in densely vegetation covered seasons. Moreover, when the growing season lasts longer, the superiority of PATC lasts longer (see in Fig. 9(b)). When there are two growing seasons in one year, the difference of the performances of PATC among different NDVI values is similar to those in Fig. 9(a)&(b), i.e., the superiority of PATC is obvious in densely vegetation covered seasons and unobvious in sparsely vegetation covered seasons (see in Fig. 9(c)&(d)). In the urban area, the annual change rate of NDVI is small. Even though PATC sometimes performs better than ATCE in summer, it also performs poorer than ATCE sometimes, which indicates a less robustness of PATC over urban area (see in Fig. 9(e)&(f)). These pixels are all obtained from plain of which the elevations are all lower than 100 m. Hence, we also selected two pixels of grassland which located in complex terrain, the elevations of which are higher than 100 m. As shown in Fig. 9(g)&(h), the superiority of PATC lasts during the growing season of vegetation. In addition, PATC also performs better than ATCE in winter of which the NDVI is low, which indicates the better performance of PATC is because that PATC can well simulates the temperature fluctuations caused by local weather change.

In summary, above results indicate a superior performance of PATC compared with ATCE, especially during the growing season of vegetation in the daytime. Moreover, PATC can also well simulate the temperature fluctuations caused by local weather change when the vegetation is sparsely covered.

V. DISCUSSION

This section aims to discuss the performance of PATC under different observations and the influence of filtered NDVI on the model performance. In this section, six pixels are randomly selected from different land cover types, of which two pixels are cropland, and other four pixels are forest, grassland, savanna and urban, respectively. For each pixel, we randomly selected 12, 16, 20, 40, 80 and 160 observations, then used the least squares fitting to compute model parameters of the temperature cycle model with the selected observations. To prevent that almost observations are in same month that leads to the ATC models cannot catch the variation of LSTs at annual scale, we made sure that every seasons all have randomly selected observations, especially when the observations are less than 20. According to the simulation results, the fitting accuracy of the temperature cycle model is gradually improved with the increase of observations. As shown in Fig. 10, the RMSE of PATC is smaller than that of ATCE and ATC under different observations wherein the ATC model has the lowest accuracy. In addition, the accuracies of ATC and ATCE change slightly with the observation counts. The difference between the highest and lowest accuracy of ATC is 0.3 K, and that of ATCE is 0.4 K, while that of PATC is 1.0 K. When the observation count is 12, the accuracy of PATC is close to that of ATCE, with a difference of 0.05 K. However, when the observation count increases to 16, the accuracy of PATC is significantly higher than that of ATCE, with a difference of 0.7 K. However, with the subsequent increase of the observations, the accuracy of PATC only fluctuates slightly. Even though more observations can bring better performance of PATC, sixteen observations are sufficient to present the performance of PATC.

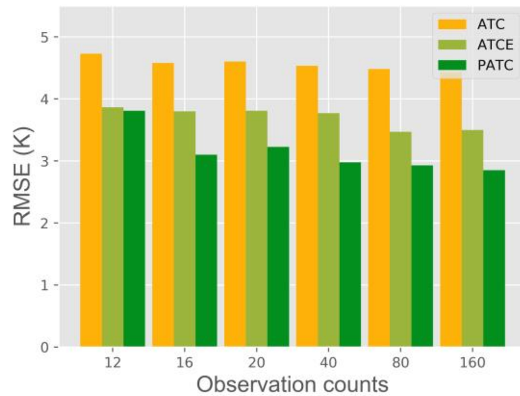

Fig. 10. RMSE of different ATC models with different observations.

In addition, we also discuss the influence of filtered NDVI on the model performance. In this section, in addition to using the filtered NDVI sequence to test the performance of temperature cycle model, we also use unfiltered NDVI as control group. As shown in Fig. 11, the influences of filtered NDVI and not filtered NDVI on PATC vary with different observation counts. As shown in Fig. 11(a), when the observation count is small, the filtered NDVI can slightly improve PATC's accuracy, but when the observation count increases, the filtered NDVI has a poorer accuracy than the unfiltered NDVI. In addition, when the NDVI change is complex in a year, the filtered NDVI losing too much information will lead to a poorer performance of PATC compared with the unfiltered NDVI (see Fig. 11(b)). Although whether the NDVI is filtered or not has a small influence on PATC totally, when the observations reach to sixteen, the filtered NDVI can increase the accuracy by 0.14 K on average compared with the unfiltered NDVI.

Compared with PATC, the filtered NDVI has a greater influence on ATCE model. As shown in Fig. 12, the filtered NDVI can improve the accuracy of ATCE by 0.1 K on average compared with the unfiltered NDVI, while for the PATC, the filtered NDVI even reduce the accuracy of PATC by 0.02 K compared with the unfiltered NDVI. This is because the ATCE puts the influence of NDVI on temperature into the local fluctuation of temperature, so the local fluctuation of NDVI has a greater influence on the ATCE. On the contrary, the PATC puts the influence of NDVI on temperature into the annual oscillation of the temperature cycle model, so the local NDVI fluctuation has less influence on the PATC.

In conclusion, above model tests suggest that PATC is robust to the filtered or not filtered NDVI sequences. Moreover, a limited observation with a count reaches to sixteen can well present the performance of PATC, which indicates a promising application of PATC in LSTs of polar satellites, such as Landsat.

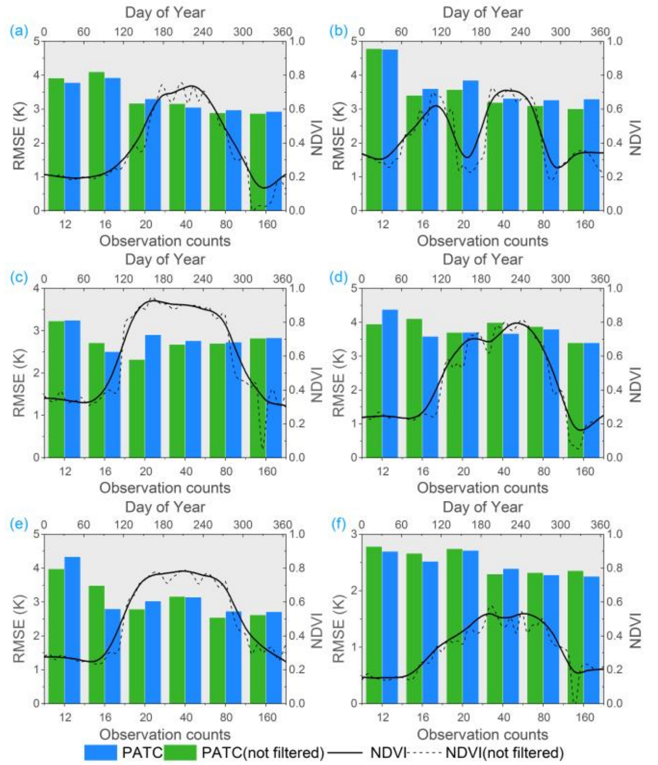

Fig. 11. RMSEs of PATC with different observations. (a): cropland 1; (b): cropland 2; (c): forest; (d): grassland; (e) savanna; (f): urban.

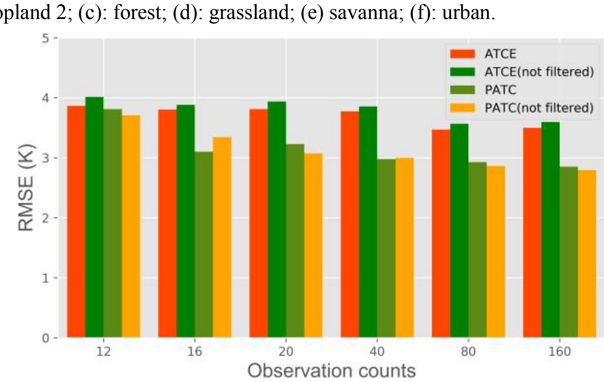

Fig. 12. RMSEs of ATCE and PATC with different observations.

VI. CONCLUSION

In this study, we propose a phenology-based ATC model (PATC) that takes the impacts of vegetation phenology and local weather changes into account. This model is based on a linear hybrid model of temperature. It is assumed that the temperature of the mixed pixel is composed of linear mixture of vegetation fractions and non-vegetation fractions, as well as short-term fluctuations caused by local weather conditions.

Here, we use MODIS LSTs to evaluate the performance of PATC and compare it with the classical ATC model and ATCE model. Compared with the classic ATC model, PATC can improve the accuracy by 1.6 K and 0.5 K in the daytime and nighttime, respectively. Compared with ATCE model, PATC can improve the mean accuracy by 0.3 K and 0.1 K in daytime and nighttime, respectively. Specifically, the superiority of PATC compared with ATCE is especially obvious during the densely vegetation covered seasons in the daytime, the Drmse of which the corresponding NDVI ranging from 0.8 to 1.0 is 1.3 K. Comparisons with ATC and ATCE suggest the superiority of PATC in modeling daily LSTs.

In addition, with the selected samples, we find the performance of PATC is robust when the number of observations reaches to sixteen, and the filtered NDVI can also slightly improve the performance of PATC when the observation count is sixteen. Future research may incorporate Landsat observations and diurnal temperature cycle (DTC) models to implement temporal interpolation of LSTs at diurnal scale.

ACKNOWLEDGMENT

The authors would like to thank the anonymous reviewers for helping improve this manuscript.

REFERENCE

[1] M. C. Anderson, R. G. Allen, A. Morse, and W. P. Kustas, "Use of Landsat thermal imagery in monitoring evapotranspiration and managing water resources," *Remote Sens. Environ,* vol. 122, pp. 50-65, 2012.

[2] S. Stisen, I. Sandholt, A. Nørgaard, R. Fensholt, and K. H. Jensen, "Combining the triangle method with thermal inertia to estimate regional evapotranspiration — Applied to MSG-SEVIRI data in the Senegal River basin," *Remote Sens. Environ,* vol. 112, no. 3, pp. 1242-1255, 2008.

[3] C. Cammalleri *et al.*, "Applications of a remote sensing-based two-source energy balance algorithm for mapping surface fluxes without in situ air temperature observations," *Remote Sensing of Environment,* vol. 124, pp. 502-515, 2012.

[4] J. Quan, Y. Chen, W. Zhan, J. Wang, J. Voogt, and M. Wang, "Multi-temporal trajectory of the urban heat island centroid in Beijing, China based on a Gaussian volume model," *Remote Sensing of Environment,* vol. 149, pp. 33-46, 2014.

[5] Q. Meng, L. Zhang, Z. Sun, F. Meng, L. Wang, and Y. Sun, "Characterizing spatial and temporal trends of surface urban heat island effect in an urban main built-up area: A 12-year case study in Beijing, China," *Remote Sensing of Environment,* vol. 204, pp. 826-837, 2017.

[6] H. Xia, Y. Chen, and J. Quan, "A simple method based on the thermal anomaly index to detect industrial heat sources," *International Journal of Applied Earth Observation and Geoinformation,* vol. 73, pp. 627-637, 2018.

[7] L. Sun *et al.*, "Reconstructing daily clear-sky land surface temperature for cloudy regions from MODIS data," *Computers & Geosciences,* vol. 105, pp. 10-20, 2017.

[8] W. L. Crosson, M. Z. Al-Hamdan, S. N. J. Hemmings, and G. M. Wade, "A daily merged MODIS Aqua–Terra land surface temperature data set for the conterminous United States," *Remote Sensing of Environment,* vol. 119, pp. 315-324, 2012.

[9] S.-B. Duan, Z.-L. Li, and P. Leng, "A framework for the retrieval of all-weather land surface temperature at a high spatial resolution from polar-orbiting thermal infrared and passive microwave data," *Remote Sensing of Environment,* vol. 195, pp. 107-117, 2017.

[10] X. Zhang, J. Zhou, S. Liang, and D. Wang, "A practical reanalysis data and thermal infrared remote sensing data merging (RTM) method for reconstruction of a 1-km all-weather land surface temperature," *Remote Sensing of Environment,* 2021.

[11] C. Zhang, W. Li, and D. Travis, "Gaps-fill of SLC-off Landsat ETM+ satellite image using a geostatistical approach," *International Journal of Remote Sensing,* vol. 28, no. 22, pp. 5103-5122, 2007.

[12] F.-W. Chen and C.-W. Liu, "Estimation of the spatial rainfall distribution using inverse distance weighting (IDW) in the middle of Taiwan," *Paddy and Water Environment,* vol. 10, no. 3, pp. 209-222, 2012.

[13] Z. Liu, P. Wu, S. Duan, W. Zhan, X. Ma, and Y. Wu, "Spatiotemporal Reconstruction of Land Surface Temperature Derived From FengYun Geostationary Satellite Data," *IEEE Journal of Selected Topics in Applied Earth Observations and Remote Sensing,* vol. 10, no. 10, pp. 4531-4543, 2017.

[14] L. Ke, X. Ding, and C. Song, "Reconstruction of Time-Series MODIS LST in Central Qinghai-Tibet Plateau Using Geostatistical Approach," *IEEE Geoscience & Remote Sensing Letters,* vol. 10, no. 6, pp. 1602-1606, 2013.

[15] X.-M. Fan, H.-G. Liu, G.-H. Liu, and S.-B. Li, "Reconstruction of MODIS land-surface temperature in a flat terrain and fragmented

landscape," *International Journal of Remote Sensing,* vol. 35, no. 23, pp. 7857-7877, 2014.

[16] J. Chen, X. Zhu, J. E. Vogelmann, F. Gao, and S. Jin, "A simple and effective method for filling gaps in Landsat ETM+ SLC-off images," *Remote Sensing of Environment,* vol. 115, no. 4, pp. 1053-1064, 2011.

[17] X. Zhu, D. Liu, and J. Chen, "A new geostatistical approach for filling gaps in Landsat ETM+ SLC-off images," *Remote Sensing of Environment,* vol. 124, pp. 49-60, 2012.

[18] C. Zeng, H. Shen, and L. Zhang, "Recovering missing pixels for Landsat ETM+ SLC-off imagery using multi-temporal regression analysis and a regularization method," *Remote Sensing of Environment,* vol. 131, pp. 182-194, 2013.

[19] T. Shuai *et al.*, "A Spectral Angle Distance-Weighting Reconstruction Method for Filled Pixels of the MODIS Land Surface Temperature Product," *IEEE Geoscience & Remote Sensing Letters,* vol. 11, no. 9, pp. 1514-1518, 2014.

[20] C. Zeng, D. Long, H. Shen, P. Wu, Y. Cui, and Y. Hong, "A two-step framework for reconstructing remotely sensed land surface temperatures contaminated by cloud," *ISPRS Journal of Photogrammetry and Remote Sensing,* vol. 141, pp. 30-45, 2018.

[21] Z. Chao, S. Huanfeng, Z. Mingliang, Z. Liangpei, and W. Penghai, "Reconstructing MODIS LST Based on Multitemporal Classification and Robust Regression," *IEEE Geoscience & Remote Sensing Letters,* vol. 12, no. 3, pp. 512-516, 2015.

[22] D. J. Weiss, P. M. Atkinson, S. Bhatt, B. Mappin, S. I. Hay, and P. W. Gething, "An effective approach for gap-filling continental scale remotely sensed time-series," *ISPRS Journal of Photogrammetry and Remote Sensing,* vol. 98, pp. 106-118, Dec 2014.

[23] Z. Liu *et al.*, "Balancing prediction accuracy and generalization ability: A hybrid framework for modelling the annual dynamics of satellite-derived land surface temperatures," *ISPRS Journal of Photogrammetry and Remote Sensing,* vol. 151, pp. 189-206, 2019.

[24] X. Li, Y. Zhou, G. R. Asrar, and Z. Zhu, "Creating a seamless 1 km resolution daily land surface temperature dataset for urban and surrounding areas in the conterminous United States," *Remote Sensing of Environment,* vol. 206, pp. 84-97, 2018.

[25] P. Fu and Q. Weng, "Temporal Dynamics of Land Surface Temperature From Landsat TIR Time Series Images," *IEEE Geoscience & Remote Sensing Letters,* vol. 12, no. 10, pp. 2175-2179, 2015.

[26] H. Ghafarian Malamiri, I. Rousta, H. Olafsson, H. Zare, and H. Zhang, "Gap-Filling of MODIS Time Series Land Surface Temperature (LST) Products Using Singular Spectrum Analysis (SSA)," *Atmosphere,* vol. 9, no. 9, 2018.

[27] P. Gething *et al.*, "Global Data for Ecology and Epidemiology: A Novel Algorithm for Temporal Fourier Processing MODIS Data," *PloS one,* vol. 3, no. 1, 2008.

[28] F. Aires, C. Prigent, and W. B. Rossow, "Temporal interpolation of global surface skin temperature diurnal cycle over land under clear and cloudy conditions," *Journal of Geophysical Research: Atmospheres,* vol. 109, no. D4, 2004.

[29] B. Bechtel, "Robustness of Annual Cycle Parameters to Characterize the Urban Thermal Landscapes," *IEEE Geoscience & Remote Sensing Letters,* vol. 9, no. 5, pp. 876-880, 2012.

[30] Y. Xu and Y. Shen, "Reconstruction of the land surface temperature time series using harmonic analysis," *Computers & Geosciences,* vol. 61, pp. 126-132, 2013.

[31] Q. Weng and P. Fu, "Modeling annual parameters of clear-sky land surface temperature variations and evaluating the impact of cloud cover using time series of Landsat TIR data," *Remote Sensing of Environment,* vol. 140, pp. 267-278, 2014.

[32] D. Sun and R. T. Pinker, "Implementation of GOES-based land surface temperature diurnal cycle to AVHRR," *INT J Remote Sens,* vol. 26, no. 18, pp. 3975-3984, 2005.

[33] F.-M. Göttsche and F.-S. Olesen, "Modelling the effect of optical thickness on diurnal cycles of land surface temperature," *Remote Sensing of Environment,* vol. 113, no. 11, pp. 2306-2316, 2009.

[34] J. Zhou, Y. Chen, X. Zhang, and W. Zhan, "Modelling the diurnal variations of urban heat islands with multi-source satellite data," *International Journal of Remote Sensing,* vol. 34, no. 21, pp. 7568-7588, 2013.

[35] J. Quan, Y. Chen, W. Zhan, J. Wang, J. Voogt, and J. Li, "A hybrid method combining neighborhood information from satellite data with modeled diurnal temperature cycles over consecutive days," *Remote Sensing of Environment,* vol. 155, pp. 257-274, 2014.

[36] F. Hong *et al.*, "Comprehensive assessment of four-parameter diurnal land surface temperature cycle models under clear-sky," *ISPRS Journal of Photogrammetry and Remote Sensing,* vol. 142, pp. 190-204, 2018.

[37] W. Zhan *et al.*, "Interpolating diurnal surface temperatures of an urban facet using sporadic thermal observations," *Building and Environment,* vol. 57, pp. 239-252, 2012.

[38] F. Huang, W. Zhan, S.-B. Duan, W. Ju, and J. Quan, "A generic framework for modeling diurnal land surface temperatures with remotely sensed thermal observations under clear sky," *Remote Sensing of Environment,* vol. 150, pp. 140-151, 2014.

[39] H. Xia, Y. Chen, Y. Li, and J. Quan, "Combining kernel-driven and fusion-based methods to generate daily high-spatial-resolution land surface temperatures," *Remote Sensing of Environment,* vol. 224, pp. 259-274, 2019.

[40] J. Quan, W. Zhan, T. Ma, Y. Du, Z. Guo, and B. Qin, "An integrated model for generating hourly Landsat-like land surface temperatures over heterogeneous landscapes," *Remote Sensing of Environment,* vol. 206, pp. 403-423, 2018.

[41] F. Huang *et al.*, "Temporal upscaling of surface urban heat island by incorporating an annual temperature cycle model: A tale of two cities," *Remote Sensing of Environment,* vol. 186, pp. 1-12, 2016.

[42] H. Liu and Q. Weng, "Enhancing temporal resolution of satellite imagery for public health studies: A case study of West Nile Virus outbreak in Los Angeles in 2007," *Remote Sensing of Environment,* vol. 117, pp. 57-71, 2012.

[43] J. Quan, W. Zhan, Y. Chen, M. Wang, and J. Wang, "Time series decomposition of remotely sensed land surface temperature and investigation of trends and seasonal variations in surface urban heat islands," *Journal of Geophysical Research: Atmospheres,* vol. 121, no. 6, pp. 2638-2657, 2016.

[44] B. Bechtel and P. Sismanidis, "Time series analysis of moderate resolution land surface temperatures," in *Remote Sensing Time Series Image Processing*: CRC Press, 2017, pp. 111-142.

[45] P. Fu and Q. Weng, "Consistent land surface temperature data generation from irregularly spaced Landsat imagery," *Remote Sensing of Environment,* vol. 184, pp. 175-187, 2016.

[46] Z. Zou *et al.*, "Enhanced Modeling of Annual Temperature Cycles with Temporally Discrete Remotely Sensed Thermal Observations," *Remote Sensing,* vol. 10, no. 4, p. 650, 2018.

[47] Z. Wan, "New refinements and validation of the collection-6 MODIS land-surface temperature/emissivity product," *Remote Sensing of Environment,* vol. 140, pp. 36-45, 2014.

[48] S.-B. Duan *et al.*, "Validation of Collection 6 MODIS land surface temperature product using in situ measurements," *Remote Sensing of Environment,* vol. 225, pp. 16-29, 2019.

[49] H. Li *et al.*, "Temperature-Based and Radiance-Based Validation of the Collection 6 MYD11 and MYD21 Land Surface Temperature Products Over Barren Surfaces in Northwestern China," *IEEE Transactions on Geoscience and Remote Sensing,* vol. 59, no. 2, pp. 1794-1807, 2021.

[50] W. H. Press, B. P. Flannery, S. A. Teukolsky, and W. T. Vetterling, *Numerical Recipes in C*. Cambridge, New York, USA: Cambridge University Press, 1990.

[51] C. Deng and C. Wu, "Examining the impacts of urban biophysical compositions on surface urban heat island: A spectral unmixing and thermal mixing approach," *Remote Sensing of Environment,* vol. 131, pp. 262-274, 2013.

[52] W. Zhu, Y. Pan, H. He, L. Wang, M. Mou, and J. Liu, "A Changing-Weight Filter Method for Reconstructing a High-Quality NDVI Time Series to Preserve the Integrity of Vegetation Phenology," *IEEE Transactions on Geoscience and Remote Sensing,* vol. 50, no. 4, pp. 1085-1094, 2012.

[53] S. Peng *et al.*, "Surface urban heat island across 419 global big cities," *Environmental Science & Technology,* vol. 46, no. 2, pp. 696-703, Jan 17 2012.

[54] J. Nichol, "Remote Sensing of Urban Heat Islands by Day and Night," *Photogrammetric Engineering & Remote Sensing,* vol. 71, no. 5, pp. 613-622, 2005.

[55] A. Chudnovsky, E. Ben-Dor, and H. Saaroni, "Diurnal thermal behavior of selected urban objects using remote sensing measurements," *Energy and Buildings,* vol. 36, no. 11, pp. 1063-1074, 2004.

This article has been accepted for publication in a future issue of this journal, but has not been fully edited. Content may change prior to final publication. Citation information: DOI 10.1109/JSTARS.2021.3085342, IEEE Journal of Selected Topics in Applied Earth Observations and Remote Sensing

Haiping Xia received a B.S. in geographic information system from School of Environment Science and Spatial Informatics, China University of Mining and Technology, Xuzhou, China, in 2015.

She is currently pursuing the Ph.D. degree with the State Key Laboratory of Remote Sensing Science, Faculty of Geographical Science, Beijing Normal University, Beijing, China. Her research interests include thermal sharpening and analysis on urban thermal environment.

Yunhao Chen received the B.S. and M.S. degrees in resource management from the Anhui University of Science and Technology, Huainan, China, in 1994 and 1997, respectively, and the Ph.D. degree in geodetic engineering from the China University of Mining and Technology, Beijing, China, in 1999.

From 2000 to 2001, he did postdoctoral research with Beijing Normal University, Beijing. Since 2001, he has been with the Faculty of Geographical Science, Beijing Normal University, where he is currently a Professor with the State Key Laboratory of Remote Sensing Science. His research interests include thermal remote sensing of urban environment and applications of remote sensing in ecology.

Adu Gong received the B.S. degree in land use and land planning from Southwest University, Chongqing, China, in 1998, the M.S. degree in soil and water conservation from Chinese Academy of Sciences / Ministry of Water Resources Chengdu Institute of Mountain Hazards and Environment, Chengdu, China, in 2001, and the Ph.D. degree in geography from Beijing Normal University, Beijing, China, in 2005.

He is currently an Associate Professor with the Faculty of Geographical Science and State Key Laboratory of Remote Sensing Science, Beijing Normal University, Beijing. His research interests include thermal remote sensing and urban heat island.

Kangning Li received a B.S. in geographic information system from the College of Urban and Environmental Science, Northwest University, Xi'an, China, in 2016.

She is currently pursuing the Ph.D. degree with the State Key Laboratory of Remote Sensing Science, Faculty of Geographical Science, Beijing Normal University, Beijing, China. Her research interests include thermal remote sensing of urban environment.

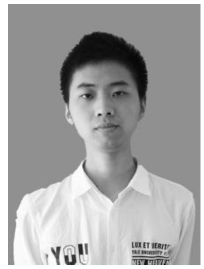

Long Liang received a B.S. in remote sensing science and technology from the School of Geosciences and Surveying Engineering, China University of Mining and Technology, Beijing, in 2018.

He is currently pursuing the Ph.D. degree with the State Key Laboratory of Remote Sensing Science, Faculty of Geographical Science, Beijing Normal University, Beijing, China. His research interests include thermal sharpening and risk assessment of natural disaster on heritages.

Zheng Guo received the B.S. degree in horticultural from China Agricultural University, Beijing, China, in 2007, the M.S. degree in ecology from Zhejiang A&F University, Zhejiang, China, in 2010, and the Ph.D. degree in geography from Beijing Normal University, Beijing, in 2013.

He is a Senior Engineer with the Division of Remote Sensing Data Application, National Satellite Meteorological Center, China Meteorological Administration, Beijing. His research interests include thermal remote sensing and applications for thermal environment of the city and atmospheric pollutants monitored by remote sensing.